Enhanced Leaching of Zinc Ferrite by the Formation of a Solid Solution With Magnetite in Hydrochloric Acid Solution

MARIAN NIDA LUMONGSOD, JONAH GAMUTAN, KAZUKI HARA, YASUSHI SASAKI, and TETSUYA NAGASAKA

The high zinc and iron contents of electric arc furnace (EAF) dust in the forms of zinc ferrite ($ZnFe_2O_4$) and magnetite (Fe_3O_4) make it a valuable secondary source of these metals. $ZnFe_2O_4$ and Fe_3O_4 are known to form a solid solution at all compositions, and while $ZnFe_2O_4$ is almost insoluble in aqueous solutions, Fe_3O_4 easily dissolves in acid. The present work investigated the enhanced leaching behavior of $ZnFe_2O_4$–Fe_3O_4 solid solutions by synthesizing a series of $(1 - x)ZnFe_2O_4$–xFe_3O_4 solid solutions, where x = mol pct Fe_3O_4, via solid-state reaction and leaching using HCl acid solution. Lattice parameter variation of the synthesized solid solutions indicated a positive deviation from Vegard's law with a maximum deviation at $x = 20$ pct Fe_3O_4. Leaching results showed that almost complete dissolution was achieved using $x = 30$ pct Fe_3O_4 solid solution at 85 °C for 2 hours. The enhanced dissolution behavior at this composition was attributed to the displacement of Zn^{2+} ions ($rZn^{2+}_{tetra} = 0.58$ Å) by the larger Fe^{2+} ions ($rFe^{2+}_{tetra} = 0.615$ Å) in the tetrahedral site of the crystal lattice, which created local distortions and strains rendering the structure vulnerable to acid attack. Therefore, with proper modification of EAF dust, the dissolution of zinc and iron can be significantly improved, which is critical towards sustainable resource recycling.

I. INTRODUCTION

In pursuit of significant energy and raw material savings and mineral resource sustainability, the global steel production by electric arc furnace (EAF) process, which uses end-of-life steel scrap as raw materials, is increasing year by year. The EAF process enables steelmaking with lower energy consumption and almost negligible gaseous emissions compared to primary steelmaking processes using basic oxygen and blast furnaces.[1] According to the World Steel Association, the global EAF steel production in 2019 was about 518 million tons,[2] which is a massive 173-million-ton increase compared to production in 2009.[3] In response to the growing demands of steel applications, worldwide EAF steel production is projected to continue to rise because of the increasing pressure to meet ever more stringent environmental regulations in the steelmaking industries.

During EAF steelmaking, about 15 to 20 kg of very fine particles called electric arc furnace (EAF) dust is generated per ton of steel produced.[4–6] This dust is categorized as a hazardous industrial waste by various government regulatory agencies due to its very fine particle size (<10 μm) and its high heavy metal content, including leachable metals such as lead, cadmium, and chromium, which can pose threats to human health and the environment.[7–11] Table I shows the typical chemical composition and mineralogy of EAF dust from various sources.[12–15] As a result, direct disposal of EAF dust to landfills is strictly prohibited, and dust treatment and management are also costly. In 2019 alone,

MARIAN NIDA LUMONGSOD is with the Department of Metallurgy, Graduate School of Engineering, Tohoku University, 6-6-02, Aoba Aramaki Aza-Aoba, Aoba-ku, Sendai 980-8579, Japan and also with the Tribology and Interfacial Chemistry (TIC) Group, SCI-STI-SM, Institute of Materials, École Polytechnique Fédérale de Lausanne, (EPFL), Station 12, CH-1015 Lausanne, Switzerland. JONAH GAMUTAN is with the Department of Metallurgy, Graduate School of Engineering, Tohoku University and also with the Minerals, Energy and Chemical Engineering, Curtin University Western Australia School of Mines, 117 Egan Street, Kalgoorlie, WA 6430, Australia. Contact e-mail: jonah.gamutan@gmail.com KAZUKI HARA is with the Department of Metallurgy, Graduate School of Engineering, Tohoku University, 6-6-02, Aoba Aramaki Aza-Aoba, Aoba-ku, Sendai 980-8579, Japan. YASUSHI SASAKI and TETSUYA NAGASAKA are with the New Industry Creation Hatchery Center, Tohoku University, 6-6-10, Aoba Aramaki Aza-Aoba, Aoba-ku, Sendai 980-8579, Japan

Elements	Zn	Fe	Pb	Cr	Cd	Al	Refs.
Composition (Mass Pct)	26.66	16.93	2.71	0.12	0.044	0.59	[12]
	24.80	32.00	1.84	—	0.03	1.03	[13]
	19.40	24.60	4.5	0.3	0.1	—	[14]
	19.02	30.0	0.99	0.34	0.04	0.53	[15]
Mineralogy	$ZnFe_2O_4$	Fe_3O_4	PbO	$FeCr_2O_4$	CdO	Al_2O_3	[12 to 15]
	ZnO	$ZnFe_2O_4$	$PbCl_2$	Cr_3O_4			
	$ZnCl_2$			CrO			

approximately 7.8 million tons of EAF dust were generated, and as EAF production continues to rise, this amount will increase correspondingly.

The EAF dust is primarily composed of zinc and iron, making it a valuable secondary source of these metals. EAF dust contains an average of 20 mass pct zinc and 30 mass pct iron[12–15] and based on this value, about 1.6 million tons of zinc and 2.4 million tons of iron could be potentially recovered from the EAF dust generated annually worldwide. Therefore, a dust treatment process to recycle these valuable metals from EAF dust is key to promoting an efficient "waste-to-raw material" strategy, thereby reducing waste disposal and minimizing the environmental impact for a circular economy.

At present, only pyrometallurgical processes based on carbothermic reduction, namely the Waelz kiln process and its variations, have reached the industrial scale in the treatment of EAF dust and recycling, particularly zinc recovery.[16–18] Challenges such as huge energy consumption, high-grade feed requirements, low thermal efficiency, large operation costs, low-value product, and greenhouse gas emissions are often encountered.[19–21] On the other hand, hydrometallurgical processes, which uses aqueous solutions to dissolve target metals into leaching solutions followed by purification and electrolysis for further refining,[22,23] are considered more environment friendly. These processes have the benefits of lower energy consumption, negligible gas emissions, and lower capital and operating costs.[24,25] EAF dust treatments by the hydrometallurgical route usually involve the use of either acidic or alkaline solutions to selectively dissolve zinc. Sulfuric acid leaching, for example, is the most used approach due to its widespread availability and relatively inexpensive cost. However, co-dissolution of iron when targeting for higher zinc dissolution, is a problem. Alkaline leaching using NaOH solutions is also widely investigated due to its selectivity to ZnO. Most of these studies, however, focus on the maximum recovery of zinc only, while iron is precipitated as hydroxides, which are of little interest to the steel industry leading to significant losses of iron.[22]

Despite the efforts to develop hydrometallurgical EAF dust treatment methods, leaching EAF dust has proven difficult due to the extremely insoluble chemical nature of its primary compound, zinc ferrite ($ZnFe_2O_4$) in both acidic and alkaline solutions.[26,27] In contrast to the insoluble characteristics of $ZnFe_2O_4$ in aqueous

solutions, another main compound, magnetite (Fe_3O_4), is rather soluble due to its weak Fe–O bonds that can be easily broken down by acid.

From the aspect of crystal structure, $ZnFe_2O_4$ and Fe_3O_4 share the same spinel structure, yet they differ in terms of their cation distribution among tetrahedral and octahedral sites. The divalent Zn^{2+} ions of a normal spinel like $ZnFe_2O_4$ occupy the tetrahedral sites, while the trivalent Fe^{3+} ions occupy the octahedral sites. On the other hand, half of the trivalent Fe^{3+} ions of an inverse spinel like Fe_3O_4 occupy the tetrahedral sites, while the divalent Fe^{2+} ions and the remaining half of the trivalent Fe^{3+} ions occupy the octahedral sites.[28–31] $ZnFe_2O_4$ and Fe_3O_4 also have very close lattice parameters with reported values of 8.396 Å and 8.4411 Å, respectively.[32,33] Due to these similarities in their crystal structure and lattice parameters, $ZnFe_2O_4$ and Fe_3O_4 are known to form a solid solution at all compositions, though a possible miscibility gap has also been proposed.[34–36]

Therefore, as part of our extensive work on EAF dust recycling,[37–43] the current work was carried out to investigate the influence of soluble Fe_3O_4 on the dissolution behavior of almost insoluble $ZnFe_2O_4$ when they form a solid solution at different compositions for the development of zinc and iron recycling technologies via hydrometallurgical processing. A series of $ZnFe_2O_4$–Fe_3O_4 solid solutions were synthesized via solid-state reaction to eliminate the influence of other elements in actual EAF dust on the leaching behavior. Then, the synthesized $ZnFe_2O_4$–Fe_3O_4 solid solutions were leached using HCl solution. This study selected HCl solution to avoid using a viscous lixiviant like H_2SO_4 and prevent the trouble associated with jarosite formation during H_2SO_4 leaching.[21,44–48]

II. EXPERIMENTAL PROCEDURES

A. $ZnFe_2O_4$-Fe_3O_4 Solid Solutions Synthesis

$ZnFe_2O_4$ was synthesized using a conventional solid-state reaction technique by heating 4-gram pelletized mixtures of reagent grade zinc oxide (ZnO) and hematite (α-Fe_2O_3) powders in a pre-heated muffle furnace at 1200 °C for 50 hours in air. Then, the samples were cooled to room temperature. Fe_3O_4 was synthesized using a gas-solid reaction method by heating reagent grade α-Fe_2O_3 powder in a horizontal furnace at
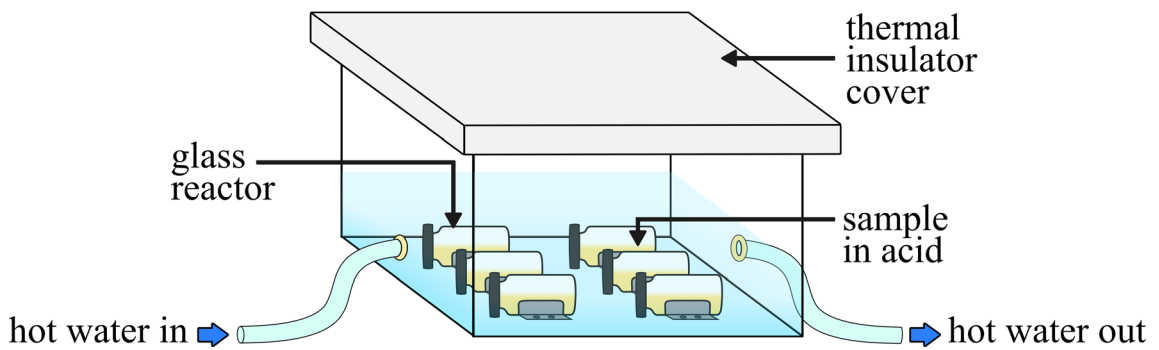
Fig. 1—Schematic diagram of the experimental set-up and leaching condition.
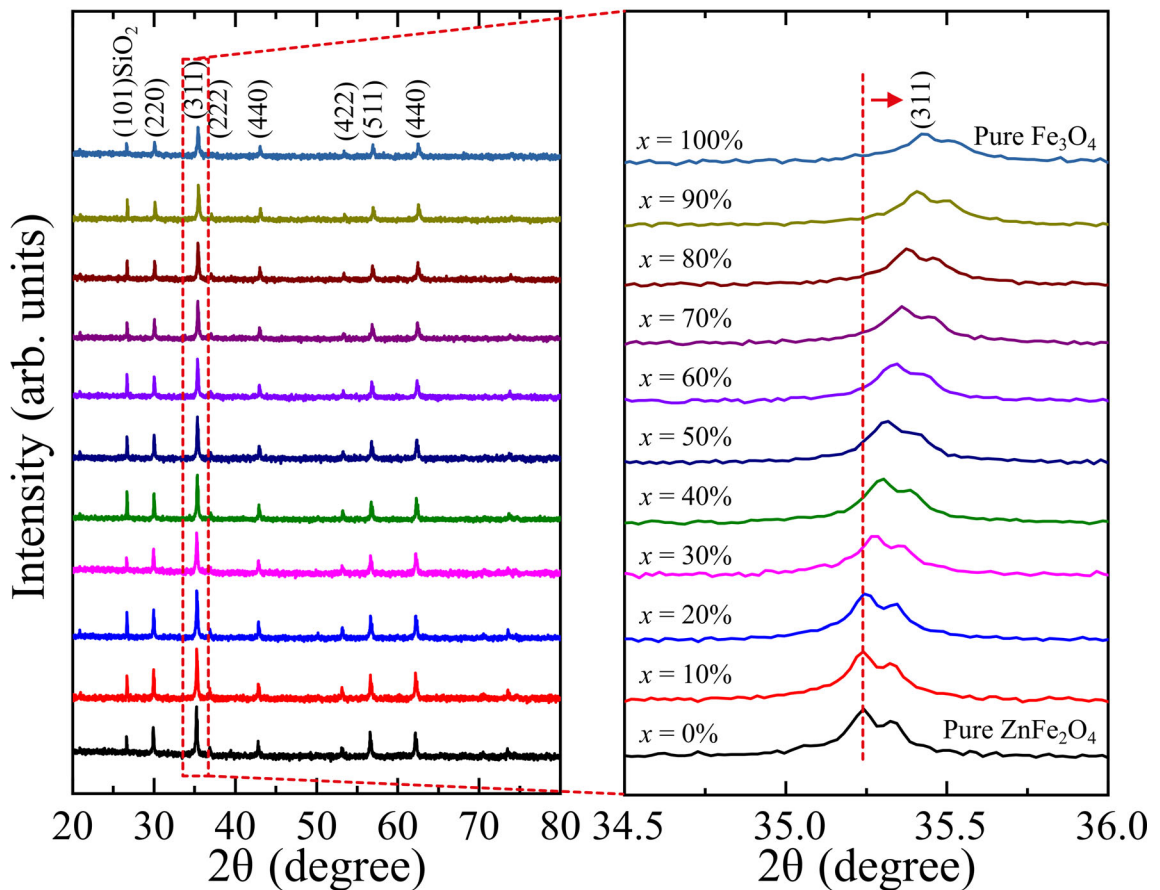
Fig. 2—XRD patterns of synthesized ZnFe$_2$O$_4$–xFe$_3$O$_4$ spinel solid solutions.

600 °C for 1 hour under CO$_2$:CO gas mixture at 70:30 volume ratio with a flow rate of 70 mL/min and 30 mL/min, respectively.

The same solid-state reaction technique was used to synthesize the $(1 − x)$ZnFe$_2$O$_4$–xFe$_3$O$_4$ spinel solid solutions. Pre-synthesized Fe$_3$O$_4$ and ZnFe$_2$O$_4$ powders were thoroughly mixed at different $x =$ mol pct Fe$_3$O$_4$,
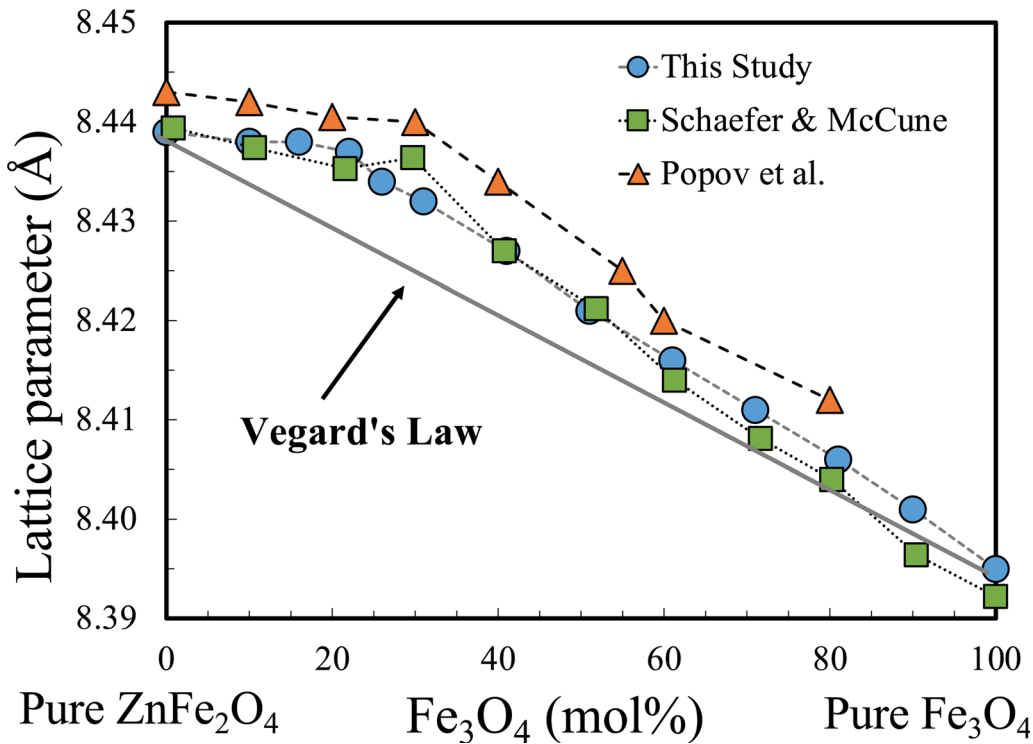
Fig. 3—Lattice parameter variation in ZnFe$_2$O$_4$–xFe$_3$O$_4$ spinel solid together with the results from Schaefer & McCune (1986) and Popov et al. (1963).[34,35]

from 0 to 100 pct at 10 pct increments. The powders were uniaxially compressed into 4-gram pellets under a pressure of 20 MPa using a hydraulic press. The heating process was carried out at 900 °C in Ar gas with a flow rate of 100 mL/min for 48 hours to provide sufficient time to achieve equilibrium and obtain homogeneous solid solutions. Flushing of the reaction chamber using Ar gas with a flow rate of 200 mL/min was done for 20 minutes before and after the heating stage to remove air and other impurities, and then rapid cooling was performed by opening the furnace top cover and immediately withdrawing the sample from the heating zone with additional direct air cooling.

B. Leaching Tests

Leaching experiments were performed in 50-mL glass reactors immersed in a constant-temperature water bath machine, as shown in Figure 1. Agitation was provided by the shaking movement of the device at a rate of 180 rpm. Leaching tests were conducted using 0.05 gram of the pulverized ZnFe$_2$O$_4$–Fe$_3$O$_4$ solid solution samples (20 to 100 μm in size) immersed in 20 ml of 1 M HCl acid solution (S/L ratio = 1/400) at 25 °C, 50 °C, and 75 °C for 15, 30, 60, and 120 minutes. A 0.05 mL sample solution was taken at pre-determined time intervals for

ICP-AES analysis, then the solution was filtered out to obtain the residue for XRD and SEM-EDS analyses. The pH values of the solutions were also measured.

C. Material Characterization

The phase composition of the synthesized ZnFe$_2$O$_4$–Fe$_3$O$_4$ solid solutions was determined using X-ray Diffraction (XRD) analysis with a Bruker Advanced D8 diffractometer. Measurements were made using monochromatic Cu Kα_1 radiation (λ = 1.540598 Å) at a scan range of 2θ = 20 to 80 deg with a step size of 0.02 deg, the scan speed of 4 deg/min, and a rotation rate of 15.0 rpm. The obtained XRD data were indexed using Rigaku PDXL Version 2 software.

Elemental analysis of the samples was carried out by an alkali fusion method followed by acid digestion. About 0.05 gram of the sample was fused with 3 grams of potassium pyrosulfate (K$_2$S$_7$O$_2$) in a platinum crucible over a Bunsen burner for about 8 minutes, or until all solids were melted. Acid digestion of the melt was carried out at 100 °C in a mixture of ultrapure water and 20 pct v/v HCl acid at 1:1 ratio until all the melt was dissolved into the solution.[41] The total zinc and iron contents of the synthesized samples were determined using Inductively Coupled Plasma-Atomic Emission Spectroscopy (ICP-AES) with a Shimadzu ICPS-8100.
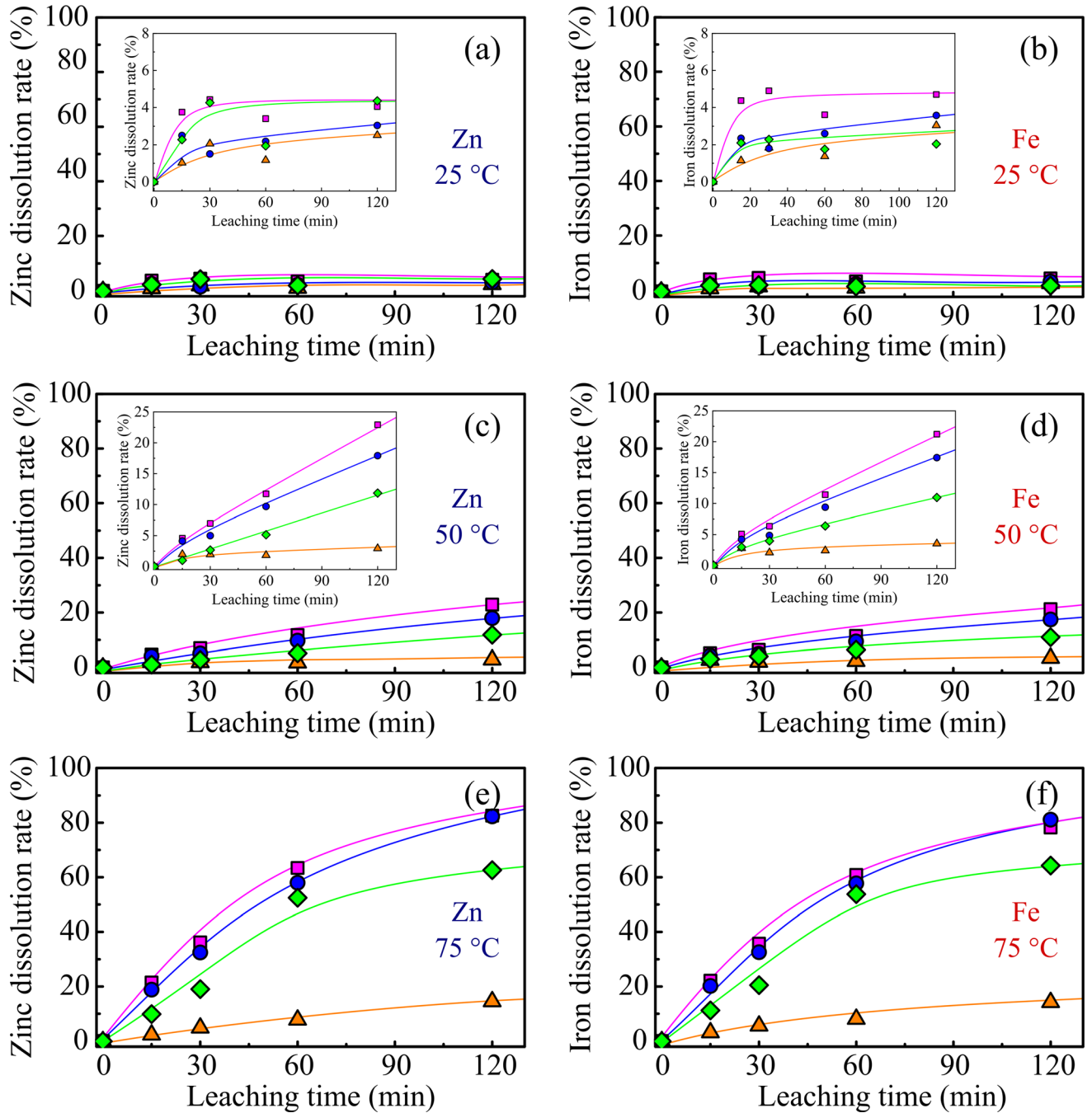
Fig. 4—Zinc (*a*, *c*, *e*) and iron (*b*, *d*, *f*) dissolution rates from ZnFe$_2$O$_4$–xFe$_3$O$_4$ spinel solid solutions, where x = mol pct Fe$_3$O$_4$, at 25, 50, and 75 °C in 1 M HCl acid.
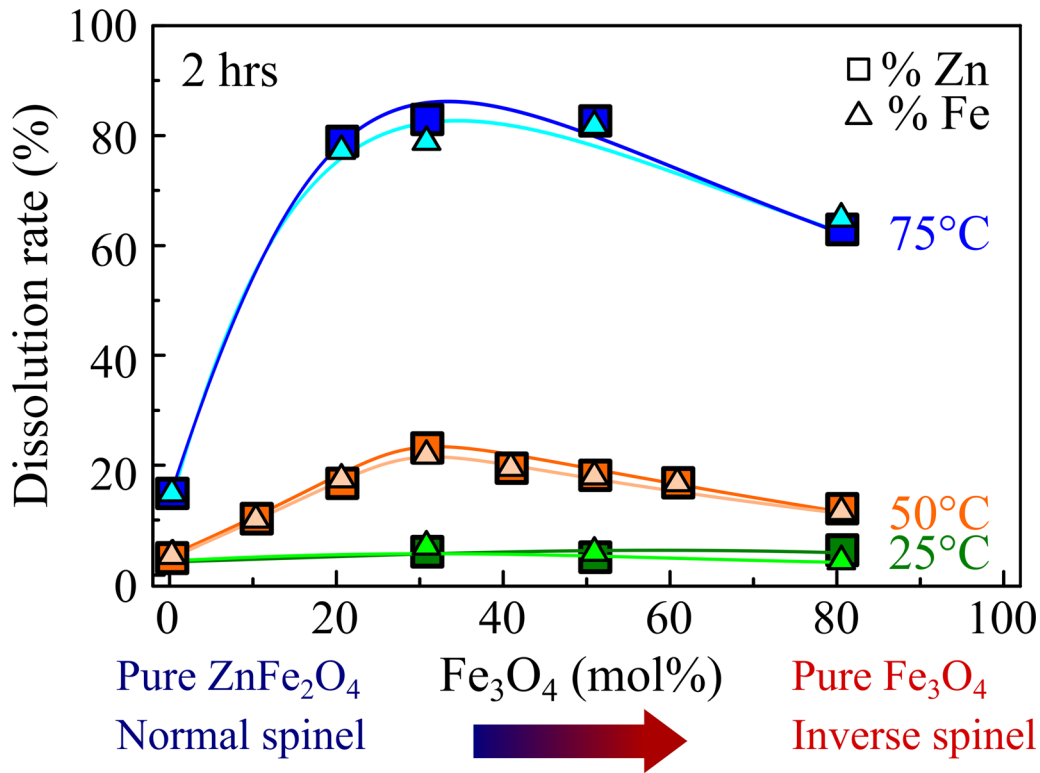
Fig. 5—The effect of Fe$_3$O$_4$ content on zinc and iron dissolution rate from ZnFe$_2$O$_4$-xFe$_3$O$_4$ spinel solid solutions, where x = mol pct Fe$_3$O$_4$, at 25, 50, and 75 °C for 2 h in 1 M HCl acid and an S/L ratio of 1/400.

III. RESULTS AND DISCUSSION

A. Synthesized $(1 - x)ZnFe_2O_4–xFe_3O_4$ Solid Solutions

X-ray diffraction patterns of the synthesized ZnFe$_2$O$_4$–Fe$_3$O$_4$ spinel solid solutions in the range of 20 to 80 deg, with reflection planes (220), (311), (222), (400), (422), (511), and (440) are shown in Figure 2. The indexing is based on the results by Swanson et al. (1967) and Swanson et al. (1971).[32,33] All the indexed peaks correspond to the characteristic planes of the Fd3m space group with cubic symmetry, confirming the formation of the single-phase ZnFe$_2$O$_4$–Fe$_3$O$_4$ solid solutions. The emergence of these peaks indicated the solubility of cations in their respective lattice sites and confirmed the formation of single-phase cubic spinel structure for all samples and that there were no other phases present.

Enlarged view of the diffraction peaks in the range of 34.5 to 36.0 deg showed a gradual shift towards larger 2θ angles with increasing Fe$_3$O$_4$ content, indicating a change in the distance between the crystal planes. From this, lattice parameters of the synthesized ZnFe$_2$O$_4$–Fe$_3$O$_4$ solid solution samples can be calculated by using Eq. [1].

$$a = \left[\frac{n\lambda}{2sin\left(\frac{2\theta_{calc}sample}{2}\right)} \right] \sqrt{h^2 + k^2 + l^2} \qquad [1]$$

where n is a positive integer (in this case, $n=1$), λ is the wavelength of the incident wave (for Cu Kα_1 radiation, $\lambda = 1.540598$ Å), $2\theta_{calc}$ is the calculated angle of (311) plane based on the peak position of standard SiO$_2$, and h, k, and l are the Miller indices of the plane.

According to Vegard's law,[49] a linear relationship exists between the crystal lattice constant of a solid solution and the concentrations of its constituents. For a binary solid solution of A and B, this relationship is expressed as given in Eq. [2][50]:

$$a_{A_xB_{1-x}} = (a_A - a_B)x + a_B \qquad [2]$$

where $a_{A_xB_{1-x}}$ is the lattice parameter of the solid solution, a_A and a_B are the lattice parameters of the pure constituents A and B, and x is the B content.

Variation in the lattice parameters of the synthesized ZnFe$_2$O$_4$-Fe$_3$O$_4$ spinel solid solutions with increasing x (mol pct Fe$_3$O$_4$) are shown in Figure 3, together with the results from Schaefer & McCune (1986) and Popov et al. (1963).[34,35] The calculated lattice parameters of the synthesized ZnFe$_2$O$_4$ (8.44 Å) and Fe$_3$O$_4$ (8.40 Å) showed excellent agreement with the standard values of each compound with reported values of 8.396 Å and 8.4411 Å, respectively.[32,33] Changes in the lattice parameters with increasing Fe$_3$O$_4$ content was also found consistent with the results from from Schaefer & McCune (1986) and Popov et al. (1963).[34,35] With increasing Fe$_3$O$_4$ content, a decrease in the lattice parameter was observed, which indicated the
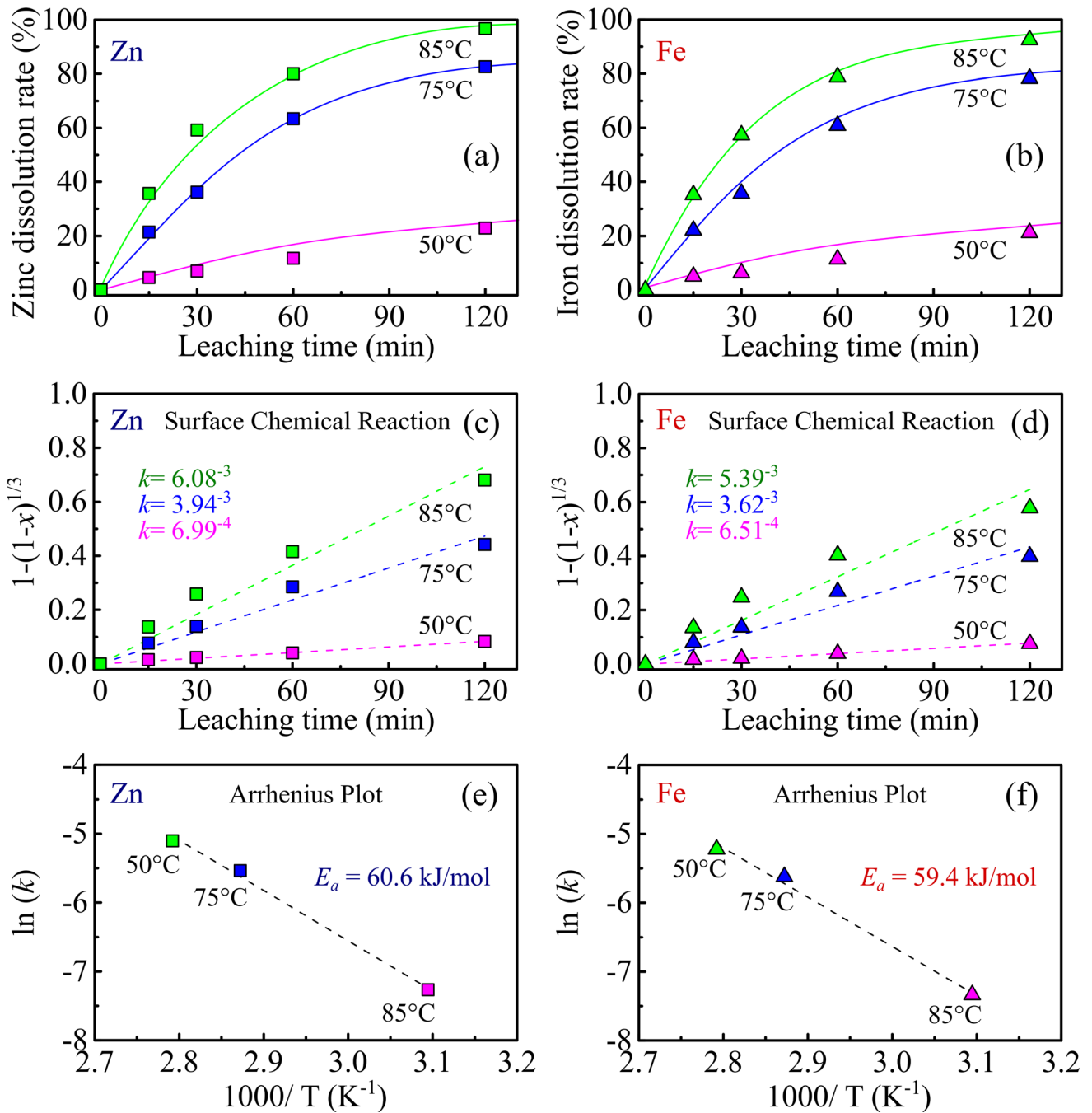
Fig. 6—The effect of temperature on (*a*) zinc and (*b*) iron dissolution rates from $ZnFe_2O_4$-30 mol pct Fe_3O_4 spinel solid solution as a function of time; kinetic plots of (*c*) zinc and (*d*) iron dissolution by surface chemical reaction control; and Arrhenius plots of (*e*) zinc and (*f*) iron dissolution.

displacement of zinc ions by smaller iron ions. Moreover, the lattice parameter variation with composition showed a positive deviation from Vegard's law, with a maximum deviation at $x = 20$ pct Fe_3O_4. The first region ($x = 0$ to 20 pct Fe_3O_4) showed a slight decrease in the lattice parameter, followed by a much more pronounced decrease from $x = 20$ to 100 pct Fe_3O_4.

B. *Leaching of Zinc and Iron from the Solid Solutions*

The zinc and iron dissolution rates of $ZnFe_2O_4$ and its solid solutions with Fe_3O_4 at various temperatures of 25 °C, 50 °C, and 75 °C are shown in Figure 4. The results show dissolution improvement of the almost insoluble $ZnFe_2O_4$ by forming a solid solution with soluble Fe_3O_4, with maximum solubility obtained from $x = 30$ pct Fe_3O_4 solid solution at all temperatures. Furthermore, Figures 4(a) and (b) show that at 25 °C,
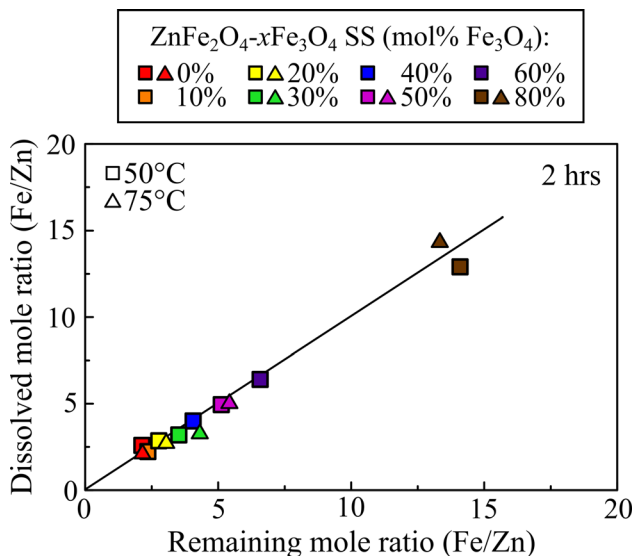
Fig. 7—Molar ratio of Fe/Zn in the solution plotted against the molar ratio of Fe/Zn in the residue after leaching at 50 and 75 °C for 2 h in 1 M HCl acid and an S/L ratio of 1/400.
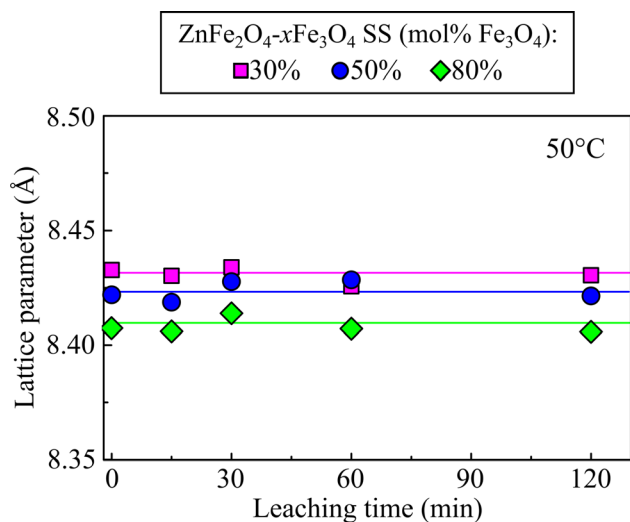

Fig. 8—Lattice parameters of $ZnFe_2O_4$–xFe_3O_4 solid solutions calculated from XRD data with x = 30, 50, and 80 mol pct Fe_3O_4 as a function of leaching time.

almost no zinc or iron was leached into the solution. However, accelerated dissolution rates were observed when increasing the temperature to 50 °C in Figures 4(c) and (d), followed by a significant increase at 75 °C in Figures 4(e) and (f), indicating that zinc and iron dissolution from $ZnFe_2O_4$–Fe_3O_4 solid solutions are temperature dependent. The leaching curves also show a progressive run with the length of time, which means that the prolongation of leaching time should result in the improvement of zinc and iron extraction.

A summary of the dissolution rates of the series of $ZnFe_2O_4$–Fe_3O_4 solid solutions after 2 hrs of leaching is shown in Figure 5. It was anticipated that there would be a continuous increase in the dissolution rates with increasing Fe_3O_4 content from hardly soluble $ZnFe_2O_4$

to soluble Fe_3O_4, but rather the leaching curves displayed two distinct regions, where a pronounced increase was observed from x = 0 to 30 pct Fe_3O_4, followed by a decrease in the rates in the second region x > 30 pct Fe_3O_4.

Focusing on the x = 30 pct Fe_3O_4 solid solution sample, the temperature dependence of zinc and iron dissolution rates at 50 °C, 75 °C, and 85 °C as a function of time is shown in Figures 6(a) and (b). These results show the significant effect of temperature and composition on the extraction of zinc and iron from the synthesized solid solutions. Although pure $ZnFe_2O_4$ barely dissolved in acid at 75 °C, nearly complete extraction was achieved from x = 30 pct Fe_3O_4 solid solution samples after leaching at 85 °C for 2 hours.

The leaching kinetics was also evaluated based on the shrinking core model as shown in Figures 6(c) and (d). It was found that the data fitted well with that of surface chemical reaction controls, indicating that the rate controlling step is the chemical reaction of H^+ ions with the solid particles on the surface of $Zn_{(1-x)}Fe_x$-Fe_2O_4 solid solutions. The activation energies of the chemical reaction were also calculated using the Arrhenius plots shown in Figures 6(e) and (f). The calculated activation energy values were 60.6 kJ/mol and 59.4 kJ/mol for zinc and iron dissolution, respectively, indicating that chemical reaction between $ZnFe_2O_4$–Fe_3O_4 solid solutions and hydrochloric acid is temperature-sensitive.

To clarify the anomalous leaching behavior at x = 30 pct Fe_3O_4, the pH of the solutions before and after leaching were also compared. At 25 °C, 50 °C, and 75 °C, the pH values of the solution before leaching were 0.32, 0.34, and 0.33, respectively. After leaching for 15, 30, 60, and 120 minutes, the pH values ranged from 0.30 to 0.32, 0.30 to 0.36, and 0.31 to 0.35, for the respective temperatures. These values indicate that the variation in the dissolution rates was not due to differing pH levels of the solutions, as revealed by the minimal changes in the pH. It could then be deduced that the anomalous improvement in zinc and iron dissolution at x = 30 pct Fe_3O_4 could be due to differences in the composition and crystal structure of the spinel under investigation.

C. Leaching Mechanism

The molar ratios of Fe/Zn in the solution and in the residue after leaching at 50 and 75 °C for 2 hours in HCl acid are shown in Figure 7. The molar ratios were found equal, suggesting that the dissolution of zinc and iron follows the stoichiometry of the solid solutions and no preference for either zinc or iron atoms takes place. XRD analysis of the leach residues also showed no other peaks apart from that coming from the $ZnFe_2O_4$-Fe_3O_4 solid solution sample, indicating that no other phases were formed during leaching. Figure 8 shows the lattice parameters of the leach residues at different leaching times, which are calculated from the strongest reflection (311) plane located around the 2θ scattering angle of 35 deg.[32,33] The results reveal that the parameters
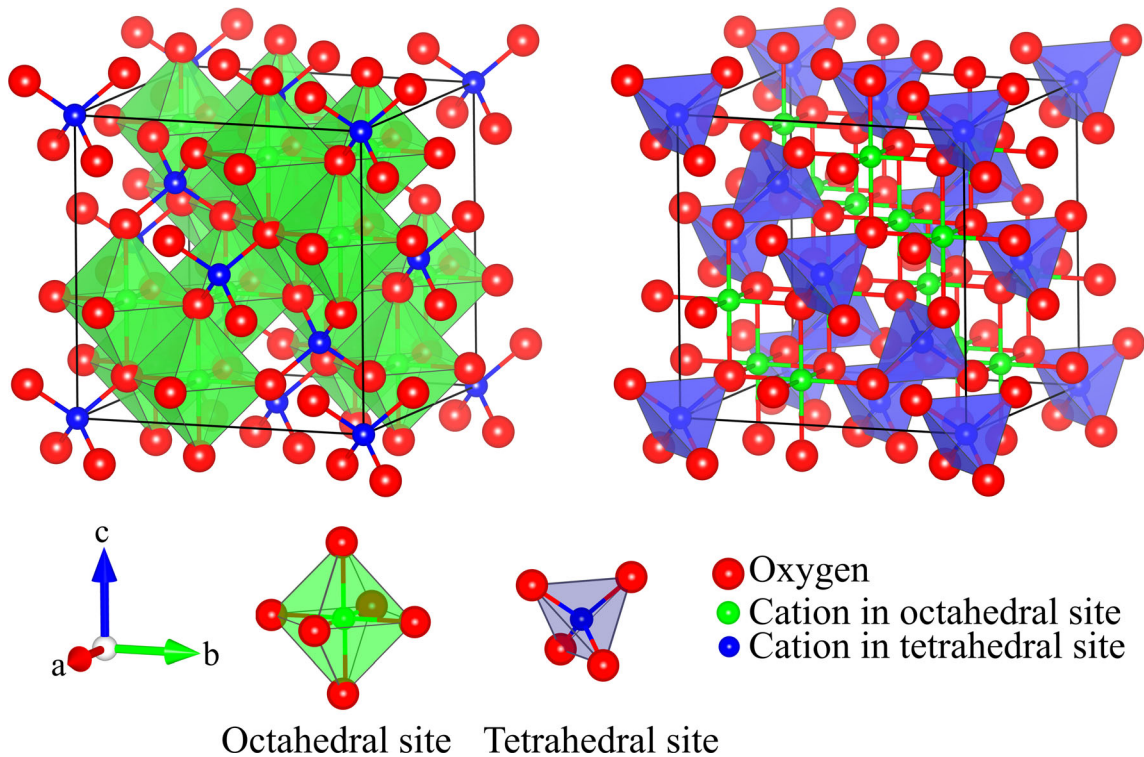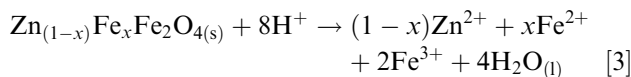
Fig. 9—The crystal structure of spinel.

remained constant, indicating that the surface of the solid retreats uniformly as the crystal dissolves during leaching.

From the above, the dissolution of the solid solutions can be described according to the following overall chemical reaction:

$$Zn_{(1-x)}Fe_xFe_2O_{4(s)} + 8H^+ \rightarrow (1-x)Zn^{2+} + xFe^{2+} \\ + 2Fe^{3+} + 4H_2O_{(l)} \quad [3]$$

The leaching mechanism characterized by the stoichiometric release of zinc and iron atoms into acid during leaching is also referred to as congruent dissolution. Since the H^+ ions from the lixiviant HCl solution react with the surface of the solid particle non-preferentially, the crystal structure should remain constant throughout the whole leaching process, which was validated by the insignificant change in the lattice parameters of the solid solutions before and after leaching shown in Figure 8.

D. Mechanism of Enhanced Dissolution

Spinels are classified into normal and inverse spinels based on the distribution of the cations among the tetrahedral and octahedral sites. A graphical representation of a spinel crystal structure showing its tetrahedral and octahedral sublattices is shown in Figure 9. In a normal spinel such as $ZnFe_2O_4$, the tetrahedral site is occupied by the divalent Zn^{2+} ion and the octahedral site is occupied by the trivalent Fe^{3+} ions. On the other hand, in the case of an inverse spinel such as pure Fe_3O_4, the tetrahedral site is occupied by half of the Fe^{3+} ions,
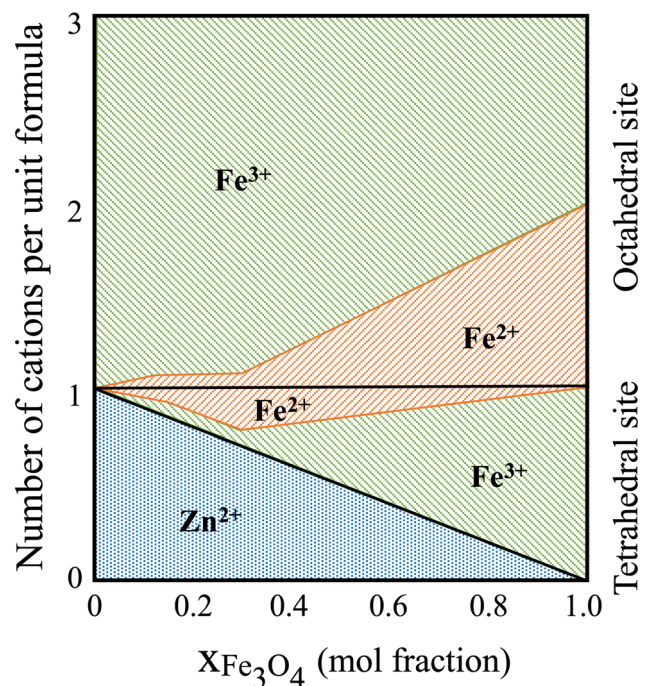

Fig. 10—Diagram of calculated site distribution of cations versus spinel composition by Graydon & Kirk (1988). Redrawn with permission from [36].

and Fe^{2+} and the remaining half of the Fe^{3+} ions occupy its octahedral site. In $ZnFe_2O_4$–Fe_3O_4 solid solutions, Zn^{2+} occupies the tetrahedral site of greatest preference because of its size and symmetrical electron

orbital. While between iron atoms, the smaller Fe^{3+} occupies the tetrahedral site with greater preference than the larger Fe^{2+}.[38–40,51–53]

It is well known that the crystal structure of $ZnFe_2O_4$–Fe_3O_4 solid solution changes from normal to inverse spinel with increasing Fe_3O_4 content, and transition occurs at around $x = 20$ to 30 pct Fe_3O_4.[34–36] Graydon and Kirk (1998) evaluated the site distribution of cations versus spinel composition in $ZnFe_2O_4$–Fe_3O_4 solid solutions as shown in Figure 10. Iron atoms in the tetrahedral site is dominated by Fe^{2+} ions when close to the proposed spinel inversion composition of $x = 20$ to 30 pct Fe_3O_4. The diameter of Fe^{2+} ions ($rFe^{2+}_{tetra} = 0.615$ Å) is significantly larger than Zn^{2+} ions ($rZn^{2+}_{tetra} = 0.58$ Å) and Fe^{3+} ions ($rFe^{3+}_{tetra} = 0.485$ Å). As a result, the Fe^{2+}–O^{2-} bond lengths in the tetrahedral site of $ZnFe_2O_4$–30 pct Fe_3O_4 become longer and weaker with the substitution of Fe^{2+}, possibly making them easier to break down during leaching. It should also be noted that in the vicinity of this composition, some large Fe^{2+} ions ($rFe^{2+}_{octa} = 0.74$ Å) are also present in the octahedral site alongside Fe^{3+} ions ($rFe^{3+}_{octa} = 0.645$ Å), making the Fe-O bonds in the octahedral site also longer and easier to collapse.

It was initially hypothesized that zinc and iron dissolution rates would increase with increasing Fe_3O_4 content from the hardly soluble $ZnFe_2O_4$ to soluble Fe_3O_4. However, it was found that the dissolution rates proceeded at an accelerated pace as it approached the proposed normal-to-inverse crystal structure transition composition, which is around $x = 20$ to 30 pct Fe_3O_4, then began to slow down as the solid solution departed farther away from that composition. It is likely that the displacement of Zn^{2+} ($rZn^{2+}_{tetra} = 0.58$ Å) by the larger Fe^{2+} ($rFe^{2+}_{tetra} = 0.615$ Å) in the tetrahedral site caused local distortions and strain in the lattice, making the structure around this composition unstable and susceptible to acid attack, thereby explaining the enhanced leaching behavior at $x = 30$ pct Fe_3O_4.

From an industrial viewpoint, these findings suggest that with proper modification of the $ZnFe_2O_4$–Fe_3O_4 solid solution found in actual EAF dust by Fe_3O_4 treatment, the dissolution of zinc and iron could be significantly improved, which is of particular interest to the steelmaking and zinc recycling industries towards a more sustainable society. In Japan where about 500,000 tons of EAF dust is generated annually, large scale application of the proposed solid solution treatment method should not be a problem. Each of the 10 EAF steelmaking companies will process an average of 50,000 tons/year or 140 kg/day of EAF dust, which is a feasible amount. Moreover, in the present work, solid solution treatment at 900 °C was intentionally carried out with a long holding time of 48 hours to compensate for equilibrium. The actual treatment time can be shortened by, for example, raising the temperature. Congruently dissolved iron and zinc ions in the solution can also be easily separated by controlling the pH of the solution. Under alkaline conditions, iron can be precipitated as $Fe(OH)_3$, while zinc stays in solution. Finally, on a broader note, the present study provides insights into the mechanism of mixing normal and inverse spinel solid solutions that is essential for processing and structural modification materials for industrial applications.

IV. CONCLUSIONS

An investigation on the dissolution behavior of synthesized $(1-x)ZnFe_2O_4$–xFe_3O_4 spinel solid solutions, where x = mol pct Fe_3O_4, was carried out to understand the influence of modifying the crystal structure on the leachability of zinc and iron from EAF dust in HCl acid solutions. It was initially hypothesized that zinc and iron dissolution rates would increase with increasing Fe_3O_4 content from the hardly soluble $ZnFe_2O_4$ to soluble Fe_3O_4. However, experimental findings showed that almost complete zinc and iron dissolution was achieved from $x = 30$ pct Fe_3O_4 solid solution after leaching at 85 °C for 2 hours. The enhanced dissolution of the $ZnFe_2O_4$–Fe_3O_4 spinel solid solution around this composition was suggested due to the proposed normal-to-inverse crystal structure transition at $x = 20$ to 30 pct Fe_3O_4 region. The presence of the much larger Fe^{2+} ions in both the tetrahedral and octahedral sites as the solid solution approaches the spinel inversion composition rendered the crystal structure unstable and resulted in longer and weaker Fe^{2+}–O bonds that were easier to break down by acid during leaching. Therefore, with proper modification of actual EAF dust by Fe_3O_4 treatment to achieve $x = 20$ to 30 pct Fe_3O_4, the dissolution of zinc and iron can be significantly improved, which is of particular interest to the steelmaking and zinc recycling industries.

CONFLICT OF INTEREST

On behalf of all authors, the corresponding author declares that there is no conflict of interest.

REFERENCES

1. World Steel Association: Fact Sheet: Steel and raw materials, 2022. Available at https://worldsteel.org/wp-content/uploads/Fact-sheet-steel-and-raw-materials.pdf (Accessed 17 April 2022).
2. World Steel Association: 2020 World steel in figures, 2020. Available at https://worldsteel.org/wp-content/uploads/2020-World-Steel-in-Figures.pdf (Accessed 18 April 2022).
3. World Steel Association: 2010 World steel in figures, 2010. Available at https://worldsteel.org/wp-content/uploads/2010-World-Steel-in-Figures.pdf (Accessed 18 April 2022).
4. P. Oustadakis, P.E. Tsakiridis, A. Katsiapi, and S. Agatzini-Leonardou: *J. Hazard. Mater.*, 2010, vol. 179, pp. 1–7.

5. A.J.B. Dutra, P.R.P. Paiva, and L.M. Tavares: *Miner. Eng.*, 2006, vol. 19, pp. 478–85.
6. T. Havlik, F. Kukurugya, D. Orac, and L. Parilak: *World Metall. ERZMETALL*, 2012, vol. 65, pp. 48–56.
7. T. Sofilić, A. Rastovčan-Mioč, Š Cerjan-Stefanović, V. Novosel-Radović, and M. Jenko: *J. Hazard. Mater.*, 2004, vol. B104, pp. 59–70.
8. C.A. Pickles: *J. Hazard. Mater.*, 2010, vol. 179, pp. 309–17.
9. J.G.M.S. Machado, F.A. Brehm, C.A.M. Moraes, C.A. Santos, A.C.F. dos Vilela, and J.B.M. da Cunha: *J. Hazard. Mater.*, 2006, vol. B136, pp. 953–60.
10. A.A. Ghani, J. Saleem, Z. Al Hameed, H. Lal, and M. Shoaib: *Pakistan J. Anal. Environ. Chem.,* 2016, vol. 17, pp. 33–7.
11. P.J.W.K. De Buzin, N.C. Heck, and A.C.F. Vilela: *J. Mater. Res. Technol.*, 2017, vol. 6, pp. 194–202.
12. N. Leclerc, E. Meux, and J.M. Lecuire: *Hydrometallurgy*, 2003, vol. 70, pp. 175–83.
13. R.A. Shawabkeh: *Hydrometallurgy*, 2010, vol. 104, pp. 61–5.
14. J. Antrekowitsch and H. Antrekowitsch: *J. Miner. Met. Mater. Soc.*, 2001, vol. 53, pp. 26–8.
15. M. Grabda, S. Oleszek-Kudlak, E. Shibata, and T. Nakamura: *J. Hazard. Mater.*, 2011, vol. 187, pp. 473–79.
16. X. Lin, Z. Peng, J. Yan, Z. Li, J.Y. Hwang, Y. Zhang, G. Li, and T. Jiang: *J. Clean. Prod.*, 2017, vol. 149, pp. 1079–1100.
17. J. Wang, Y. Zhang, K. Cui, T. Fu, J. Gao, S. Hussain, and T.S. AlGarni: *J. Clean. Prod.*, 2021, vol. 298, p. 126788.
18. R.L. Nyirenda: *Miner. Eng.*, 1991, vol. 4, pp. 1003–25.
19. S. Yamada, H. Itaya, and Y. Hara: *Iron Steel Eng.*, 1998, vol. 75, pp. 64–67.
20. L.J.H. Buitrago, I.D. Prada, G. Amaral-Labat, F. Beneduce Neto, and G.F.B.L. Silva: *Rev. Mater.*, 2018, vol. 23, pp. 343.
21. H.S. Lee and Y.Y. Teo: *IOP Conf. Ser. Earth Environ. Sci.*, 2021, vol. 945, pp. 4–11.
22. K. Binnemans P.T. Jones, Á.M. Fernández, and V.M. Torres: *J. Sustain. Metall.*, 2020, vol. 6, pp. 505–40.
23. N. Antuñano, J.F. Cambra, and P.L. Arias: *Process Saf. Environ. Prot.*, 2019, vol. 129, pp. 308–20.
24. C.A. Pickles: *J. Hazard. Mater.*, 2009, vol. 166, pp. 1030–042.
25. T. Havlik, B.V. Souza, A.M. Bernardes, I.A.H. Schneider, and A. Miskufova: *J. Hazard. Mater.*, 2006, vol. B135, pp. 311–18.
26. Š Langová and D. Matýsek: *Hydrometallurgy*, 2010, vol. 101, pp. 171–73.
27. Z. Youcai and R. Stanforth: *J. Hazard. Mater.*, 2000, vol. B80, pp. 223–40.
28. K.E. Sickafus, J.M. Wills, and N.W. Grimes: *J. Am. Ceram. Soc.*, 1999, vol. 82, pp. 4379–3292.
29. T.F.W. Barth and E. Posnjak: *Zeitschrift Für Krist*, 1931, pp. 325–41.
30. J. Smit and H.P.J. Wijn: *Ferrites*, John Wiley & Sons Ltd., New York, 1959, pp. 136–45.
31. R.J. Hill, J.R. Craig, and G.V. Gibbs: *Phys. Chem. Miner.*, 1979, vol. 4, pp. 317–39.
32. H.E. Swanson, H.F. McMurdie, M.C. Morris, and E.H. Evans: *Nat. Bur. Stand. (US)*, 1967, Monogr. 25-5, p. 31.
33. H.E. Swanson, H.F. McMurdie, M.C. Morris, E.H. Evans, and B. Paretzkin: *Nat. Bur. Stand. (US)*, 1971, Monogr. 25-9, p. 60.
34. S.C. Schaefer and R.A. McCune: *Metall. Trans. B*, 1986, vol. 17B, pp. 515–21.
35. G.P. Popov, M.I. Simonova, and T.A. Ugolnikova: *Dokl. Akad. Nauk SSSR*, 1963, vol. 148, pp. 357–60.
36. J.W. Graydon and D.W. Kirk: *Metall. Trans. B*, 1988, vol. 19B, pp. 919–25.
37. S. Itoh, A. Tsubone, K. Matsubae-Yokoyama, K. Nakajima, and T. Nagasaka: *ISIJ Int.*, 2008, vol. 48, pp. 1339–44.
38. K. Nakajima, K. Matsubae-Yokoyama, S. Nakamura, S. Itoh, and T. Nagasaka: *ISIJ Int.*, 2008, vol. 48, pp. 1478–83.
39. H.W. Ma, K. Matsubae, K. Nakajima, M.S. Tsai, K.H. Shao, P.C. Chen, C.H. Lee, and T. Nagasaka: *Resour. Conserv. Recycl.*, 2011, vol. 56, pp. 134–60.
40. A. Tsubone, T. Momiyama, M. Inoue, R. Chairaksa, K. Matsubae, T. Miki, and T. Nagasaka: *Iron Steel Technol.*, 2012, vol. 9, pp. 184–93.
41. R. Chairaksa-Fujimoto, Y. Inoue, N. Umeda, S. Itoh, and T. Nagasaka: *Int. J. Miner. Metall. Mater.*, 2015, vol. 22, pp. 788–97.
42. R. Chairaksa-Fujimoto, K. Maruyama, T. Miki, and T. Nagasaka: *Hydrometallurgy*, 2016, vol. 159, pp. 120–25.
43. T. Miki, R. Chairaksa-Fujimoto, K. Maruyama, and T. Nagasaka: *J. Hazard. Mater.*, 2016, vol. 302, pp. 90–96.
44. P. Halli, J. Hamuyuni, H. Revitzer, and M. Lundström: *J. Clean. Prod.*, 2017, vol. 164, pp. 265–76.
45. Š Langová, J. Leško, and D. Matýsek: *Hydrometallurgy*, 2009, vol. 95, pp. 179–82.
46. D.S. Baik and D.J. Fray: *Miner. Process. Extr Metall.*, 2000, vol. 109, pp. 121–28.
47. Y.Y. Teo and H.S. Lee: *AIP Conf. Proc.*, 2019, vol. 2157, pp. 2–9.
48. C. Núñez and J. Viñals: *Metall. Trans. B.*, 1984, vol. 15B, pp. 221–28. https://doi.org/10.1007/BF02667324.
49. L. Vegard and H. Dale: *Z. Krist.*, 1928, vol. 67, p. 148.
50. A.R. Denton and N.W. Ashcroft: *Phys. Rev. A*, 1991, vol. 43, pp. 3161–64.
51. J.D. Dunitz and L.E. Orgel: *J. Phys. Chem. Solids*, 1957, vol. 3, pp. 318–23.
52. A. Navrotsky and O.J. Kleppa: *J. Inorg. Nucl. Chem.*, 1967, vol. 29, pp. 2701–14.
53. K.T. Jacob and C.B. Alcock: *Metall. Trans. B*, 1975, vol. 6B, pp. 215–21.